Oxygen vacancy engineering of mesoporous Bi-Fe$_2$O$_3$@NC multi-channel microspheres for remarkable oxygen reduction and aqueous/flexible Zn-air batteries

Lixia Wang [a], Yanjing Qin [a], Huatong Li [a], Zhiyang Huang [a], Mingcheng Gao [a], Tayirjan Taylor Isimjan [b,*], Xiulin Yang [a,*]

[a] Guangxi Key Laboratory of Low Carbon Energy Materials, School of Chemistry and Pharmaceutical Sciences, Guangxi Normal University, Guilin 541004, China
[b] Saudi Arabia Basic Industries Corporation (SABIC) at King Abdullah University of Science and Technology (KAUST), Thuwal 23955-6900, Saudi Arabia

HIGHLIGHTS

- A unique multichannel Bi-Fe$_2$O$_3$@NC mesoporous catalyst was synthesized for ORR.
- Bi-Fe$_2$O$_3$@NC exhibits a higher half-wave potential and large limiting current density.
- Bi-Fe$_2$O$_3$@NC based aqueous/flexible Zn-air batteries deliver high peak power densities.
- Abundant oxygen vacancies regulate the electronic structure and provide new active sites on the catalyst surface.

GRAPHICAL ABSTRACT
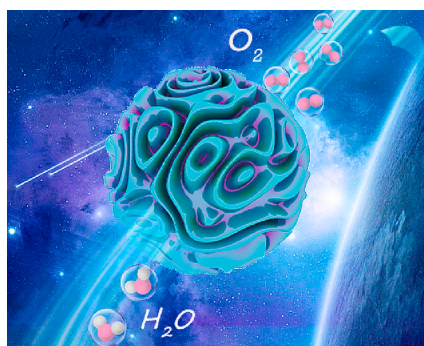
ABSTRACT

Designing multi-channel mesoporous structure and introducing oxygen vacancies to synergistically enhance oxygen reduction reaction (ORR) activity is crucial for the practical application of zinc-air batteries (ZABs) in the field of energy storage and conversion. Herein, a novel multi-channel mesoporous Bi-Fe$_2$O$_3$ microsphere with abundant oxygen vacancies supported on nitrogen-doped carbon (denoted as Bi-Fe$_2$O$_3$@NC) is constructed and the designated catalyst demonstrates a higher half-wave potential (0.88 V), large limiting current density (5.8 mA cm^{-2}@0.4 V), and superior stability. Besides, the aqueous ZAB utilizing Bi-Fe$_2$O$_3$@NC cathode achieves a high power density of 198.6 mW cm^{-2} and maintains exceptional stability for 459 h at 5 mA cm^{-2}, superior to most previously reported catalysts. Furthermore, a solid-state ZAB assembled with Bi-Fe$_2$O$_3$@NC shows a power density of 55.9 mW cm^{-2}, highlighting its potential for flexible ZAB applications. The prominent ORR performance of Bi-Fe$_2$O$_3$@NC can be ascribed to its unique multi-channel mesoporous structure and abundant oxygen vacancies, which increase the exposure of active sites and facilitate efficient electron/mass transport. This work provides valuable insights for the rational design of advanced ORR catalysts for the practical requirements of aqueous/flexible ZABs in energy storage and conversion.

1. Introduction

The ever-increasing energy demand has prompted researchers to explore and develop new technologies for clean energy storage and conversion [1–3]. Zinc-air batteries (ZABs) are considered a promising alternative power sources with the advantages of high energy density, safety and environmental benignity [4,5]. However, the energy output of these batteries is significantly limited by the slow kinetics of the oxygen reduction reaction (ORR) during discharge [6]. Typically, Pt-based materials are regarded as the most effective ORR catalysts [7]. Unfortunately, their scarcity, prohibitive cost, and poor durability severely hinder their large-scale application [8]. Therefore, there is an urgent to design and explore cost-effective, efficient, and stable non-precious metal ORR catalysts to enlarge the practical application of ZABs [9].

Recent studies have reported the effectiveness of metal oxides [10], nitrides [11], phosphides [12], and other materials as catalysts for ORR. Metal oxides, in particular, can provide chemisorption sites of oxygen molecules [13]. However, pure metal oxides exhibit low electrocatalytic activity due to their poor electrical conductivity [14]. It has been demonstrated that the construction of metal/metal oxide composites can facilitate charge redistribution between the adjacent components, resulting in enhanced electrical conductivity and accelerated charge transfer. This, in turn, optimizes the adsorption-free energy of the reaction intermediates, leading to efficient catalysis of the ORR [15]. Interestingly, introducing oxygen vacancies into pure metal oxides has shown the ability to increase the localization of metal $3d$ electrons near the Fermi level. This leads to an enhancement in carrier concentration and an improvement in the electrical conductivity of the catalyst [16,17]. Additionally, oxygen vacancies can generate defect-rich metal oxides, creating new active sites on the catalyst surface. These active sites play a crucial role in optimizing the adsorption and dissociation energy of oxygen-containing reactants, thereby significantly enhancing the catalytic activity of the material. Moreover, oxygen vacancies can also impact the stability and durability of the catalyst by preventing the aggregation and sintering of nanoparticles [18,19]. Reports suggest that coupling of metal/metal oxide catalysts with carbon materials yields admirable activity and durability [20]. Moreover, since ORR is an interfacial/surface reaction, designing and constructing catalysts with a high surface area and multi-channel pore structure is beneficial for exposing more active sites and facilitating rapid mass/charge transfer [21]. Surprisingly, the multi-channel mesoporous microsphere structure is a highly desirable morphology for enhancing electrocatalytic performance. It not only provides a large contact interface between the electrocatalyst and the electrolyte but also facilitates the rapid passage of gas [22,23]. Therefore, the design of a multi-channel mesoporous microsphere structure based on transition metal oxide composites with abundant oxygen vacancies represents a viable approach for improving electrical conductivity and enhance catalytic performance of ORR catalysts.

In this study, we prepared a Bi-Fe$_2$O$_3$@NC microsphere structure with abundant oxygen vacancies by depositing iron on the surface of BiOBr precursor, followed by high-temperature calcination. The unique surface wrinkled microsphere morphology of the catalyst results in a significantly large specific surface area and abundant porosity, promoting effective mass/charge transport. The formation of oxygen vacancies enhances the electrical conductivity of the catalyst, contributing to its improved catalytic activity. The optimal Bi-Fe$_2$O$_3$@NC displays superior ORR performance, good methanol tolerance and robust stability. Additionally, the Bi-Fe$_2$O$_3$@NC based ZAB demonstrates exceptional performance, including high peak power density of 198.6 mW cm^{-2}, high specific capacity of 774.3 mAh g$_{Zn}^{-1}$, and robust charge/discharge stability for 459 h. Notably, the flexible solid-state battery utilizing this catalyst achieves an open-circuit voltage of 1.32 V and provides a maximum power density of 55.9 mW cm^{-2}. These results confirm the great potential of Bi-Fe$_2$O$_3$@NC as an air cathode catalyst for aqueous/solid-state ZABs.

2. Experimental section

2.1. Chemicals and reagents

Bismuth nitrate pentahydrate (Bi(NO$_3$)$_3$·5H$_2$O, ≥99.0%), iron (III) chloride, anhydrous (FeCl$_3$, ≥97.0%), potassium Bromide (KBr, ≥99.0%), ethylene glycol (C$_2$H$_6$O$_2$, ≥99.5%), zinc acetate dihydrate (Zn(Ac)$_2$, 99.0%) and potassium hydroxide (KOH, 99.0%) were purchased from Guangxi Zoey Biotechnology Co., Ltd. Poly(vinylpyrrolidone) ((C$_6$H$_9$NO)$_n$, 99%, PVP), dopamine hydrochloride (C$_8$H$_{11}$NO$_2$·HCl, 98%), and tris(hydroxymethyl)aminomethane (C$_4$H$_{11}$NO$_3$, ≥99.8%) were obtained from Aladdin Industrial Corporation. Nafion (5% solution) and commercial Pt/C (20 wt% for platinum) was obtained from Alfa Aesar. The RuO$_2$ powder was prepared by calcining RuCl$_3$ in the air at 400 °C.

2.2. Synthesis of BiOBr spheres

The BiOBr spheres were obtained based on previously reported methods with slightly modification [24]. In a typical procedure, a solution was prepared by dissolving 300 mg of Bi(NO$_3$)$_3$·5H$_2$O and 3 g of PVP in 20 mL of ethylene glycol. The solution was stirred for 30 min until a clear solution was obtained. Subsequently, 100 mg KBr was added and stirred for 10 min. The resulting mixture was transferred to a Teflon-lined stainless steel autoclave (50 mL) and maintained at 150 °C for 12 h. After cooling to room temperature, the light yellow powder was subjected to several rounds of centrifugation with methanol and deionized water, and dried overnight at 60 °C.

2.3. Synthesis of BiOBr-PDA

To synthesize BiOBr-PDA, 300 mg BiOBr spheres were dissolved in 30 mL of deionized water. Sequentially, 300 mg of dopamine hydrochloride was added under sonication. Afterwards, tris-buffer solution was added to the above solution to adjusted pH approximately to 8. The resulting solution was continuously stirred for 9 h at room temperature. Then, the precursor was collected by centrifugation and dried at 60 °C, resulting in the formation of a black powder designated as BiOBr-PDA.

2.4. Synthesis of Bi-Fe$_2$O$_3$@NC

To disperse the BiOBr-PDA powder, 250 mg of the aforementioned powder was added to 30 mL of 0.2 M (0.1 M, 0.3 M) FeCl$_3$ solution with continuous stirring for 6 h at room temperature. The resulting product was washed by centrifugation and subsequently dried at 60 °C. The obtained product was then transferred to a tube furnace and then elevated to different temperatures (800, 900, 1000 °C) under N$_2$ at a heating rate of 5 °C min^{-1} to obtain Bi-Fe$_2$O$_3$@NC.

2.5. Synthesis of Bi$_2$O$_3$@NC

The Bi$_2$O$_3$@NC was obtained by direct pyrolysis of BiOBr-PDA at 900 °C for 2 h.

2.6. Synthesis of Fe-Fe$_3$O$_4$@NC

The preparation process of Fe-Fe$_3$O$_4$@NC followed a similar procedure to that of Bi-Fe$_2$O$_3$@NC, with the exception of omitting the BiOBr precursor. In detail, 300 mg of dopamine hydrochloride was dissolved in 30 mL of deionized water. The pH of the solution was adjusted to approximately 8 by adding Tris-buffer. The mixture was stirred for 9 h at room temperature, then washed, centrifuged, and dried at 60 °C. Afterwards, 250 mg of the dried powder mentioned above was added to 30 mL of 0.2 M FeCl$_3$ solution and stirred for 6 h. The resulting mixture was

subjected to centrifugation, and the black powder obtained after centrifugation was dried. Finally, the dried powder was heated at 900 °C for 2 h, resulting in the formation of Fe-Fe$_3$O$_4$@NC.

3. Results and discussion

3.1. Synthesis and structural analysis

The synthesis strategy employed for the formation of Bi-Fe$_2$O$_3$@NC microsphere structure is illustrated in Fig. 1a. Initially, BiOBr spheres were synthesized using a modified hydrothermal method. These spheres were then coated with a layer of polydopamine (PDA)-coated Fe species and subjected to high-temperature pyrolysis, resulting in the formation of the multi-channel Bi-Fe$_2$O$_3$@NC structure. The phase composition of the catalysts was determined using X-ray diffraction (XRD). As presented in Fig. S2, the diffraction peaks of BiOBr spheres match those of BiOBr (JCPDS:03–0733) [25]. In Fig. 1b, the characteristic peaks of Bi-Fe$_2$O$_3$@NC correspond well to Bi (JCPDS: 05–0519). Additionally, several strong diffraction peaks at around 30.0°, 32.2°, 35.6°, 43.5° and 62.7° can be attributed to the (220), (221), (311), (400), (511) and (440) lattice planes of Fe$_2$O$_3$ (JCPDS: 04–0755) [26], indicating the successful synthesis of Bi-Fe$_2$O$_3$@NC hybrid. Furthermore, the XRD patterns of other comparison samples are presented in Fig. S3, corresponding Fe-Fe$_3$O$_4$@NC and Bi$_2$O$_3$@NC, respectively. The Raman spectra of Bi-Fe$_2$O$_3$@NC-T (T = 800, 900, 1000 °C) exhibit two distinct peaks at 1350 cm^{-1} (D-band) and 1580 cm^{-1} (G-band) in Fig. S4a, representing the sp^2 vibration of graphitic carbon and sp^3 structural defects, respectively [27]. The maximum relative intensity ratio (I$_D$/I$_G$) values in the D and G bands were observed at 900 °C, with a value of 1.18, higher than Bi-Fe$_2$O$_3$@NC-800 (0.94) and Bi-Fe$_2$O$_3$@NC-1000 (1.12). These results indicate that the orderliness of the carbon lattice decreases and structural defects increase at an annealing temperature of 900 °C, effectively enhancing oxygen adsorption [28]. Compared to Bi-Fe$_3$O$_4$@NC (1.07) and Bi$_2$O$_3$@NC (1.03), Bi-Fe$_2$O$_3$@NC also exhibits the highest I$_D$/I$_G$, which facilitates the kinetics of ion transport (Fig. S4b) [29]. The N$_2$ adsorption–desorption isotherm was plotted in Fig. 1c to evaluate the surface area and pore volume. The Brunauer–Emmett–Teller (BET) specific surface area of Bi-Fe$_2$O$_3$@NC was approximately

393.2 m^2 g^{-1}, with an average pore size of 7.5 nm (inset in Fig. 1c). The unique mesoporous structure enables the availability of abundant active sites and promotes efficient mass/electron transfer, thereby enhancing catalytic efficiency [30]. Electron paramagnetic resonance (EPR) measurements were conducted to characterize the O vacancies in the obtained catalysts, as shown in Fig. S5 and Fig. 1d. Among the comparative catalysts, Bi-Fe$_2$O$_3$@NC exhibited a more pronounced EPR signal (g = ~2.005) at an annealing temperature of 900 °C compared to Bi$_2$O$_3$@NC (g = ~2.003) and Fe-Fe$_3$O$_4$@NC (g = ~2.005). This observation suggests the presence of a higher concentration of oxygen vacancies in the Bi-Fe$_2$O$_3$@NC catalyst [31]. It is worth noting that slight peak shifts can be influenced by the binding forces of atoms surrounding the catalyst [32,33]. The existence of unpaired electrons, induced by oxygen vacancies, can modulate the electronic structure and surface chemistry properties of the catalyst, ultimately enhancing its catalytic activity [34].

The morphology and structure of catalysts were further investigated using scanning electron microscopy (SEM) and transmission electron microscopy (TEM). The BiOBr precursor exhibited a spherical structure composed of numerous uniform nanosheets (Fig. 2a). The SEM image in Fig. 2b revealed that the obtained Bi-Fe$_2$O$_3$@NC maintained its original spherical structure even after the loading of Fe species and the calcination process. The resulting structure formed a multi-channel mesoporous architecture, facilitating electrolyte transport and providing sufficient exposure of active sites during the electrocatalytic process [35]. The microsphere structure of Bi-Fe$_2$O$_3$@NC was further confirmed by TEM (Fig. 2c). High-resolution TEM (HR-TEM) images of Bi-Fe$_2$O$_3$@NC displayed distinct lattice fringes with a spacing of 0.292 nm corresponding to the (220) plane of Fe$_2$O$_3$ and lattice fringes with a spacing of 0.248 nm consistent with the (104) plane of Bi (Fig. 2d-f). These results provide further evidence for the successful preparation of Bi-Fe$_2$O$_3$@NC microspheres. Additionally, high-angle annular dark-field scanning transmission electron microscopy (HAADF-STEM) in Fig. 2g confirmed the microsphere structure. The corresponding energy dispersive X-ray spectroscopy (EDS) pattern (Fig. S6) and elemental mapping confirmed the uniform distribution of Bi, Fe, O, C and N on the Bi-Fe$_2$O$_3$@NC structure.

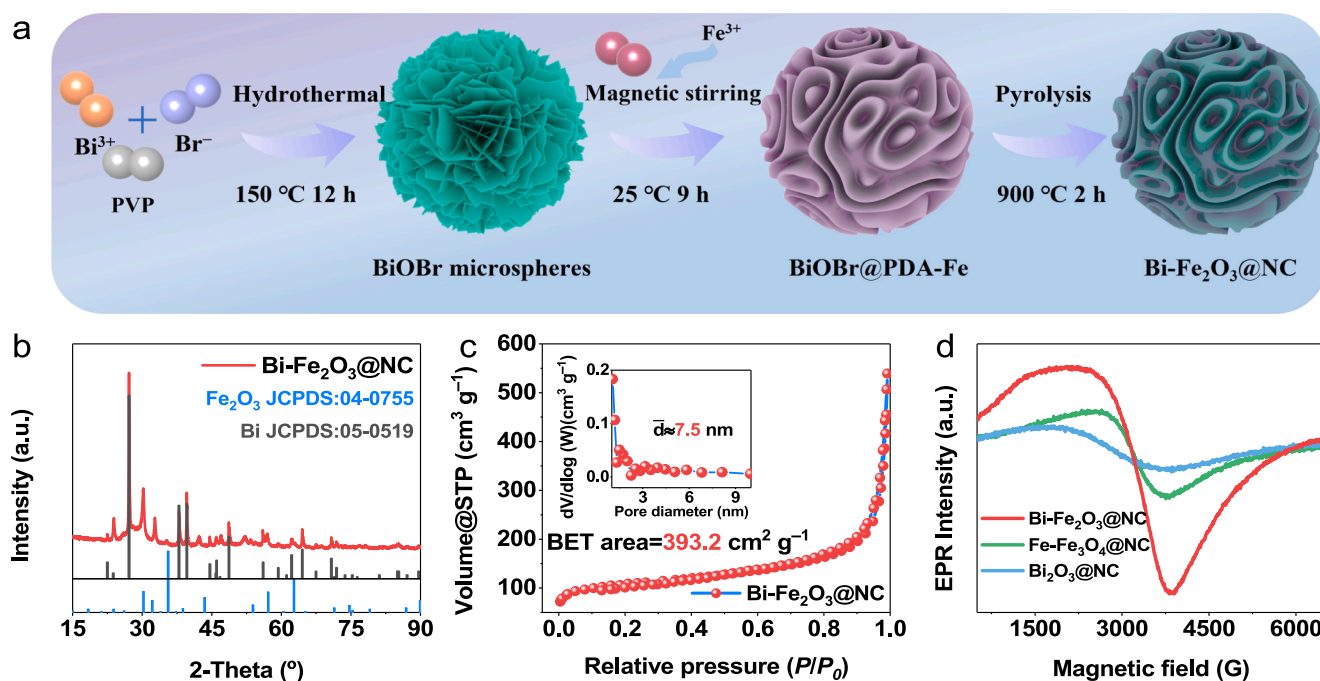To gain further insights into the electronic structure and surface

Fig. 1. (a) Schematic illustration of the synthesis process. (b) XRD pattern of Bi-Fe$_2$O$_3$@NC. (c) N$_2$ adsorption–desorption isotherm with the inset pore size distribution of Bi-Fe$_2$O$_3$@NC. (d) EPR spectra of as-synthesized samples.
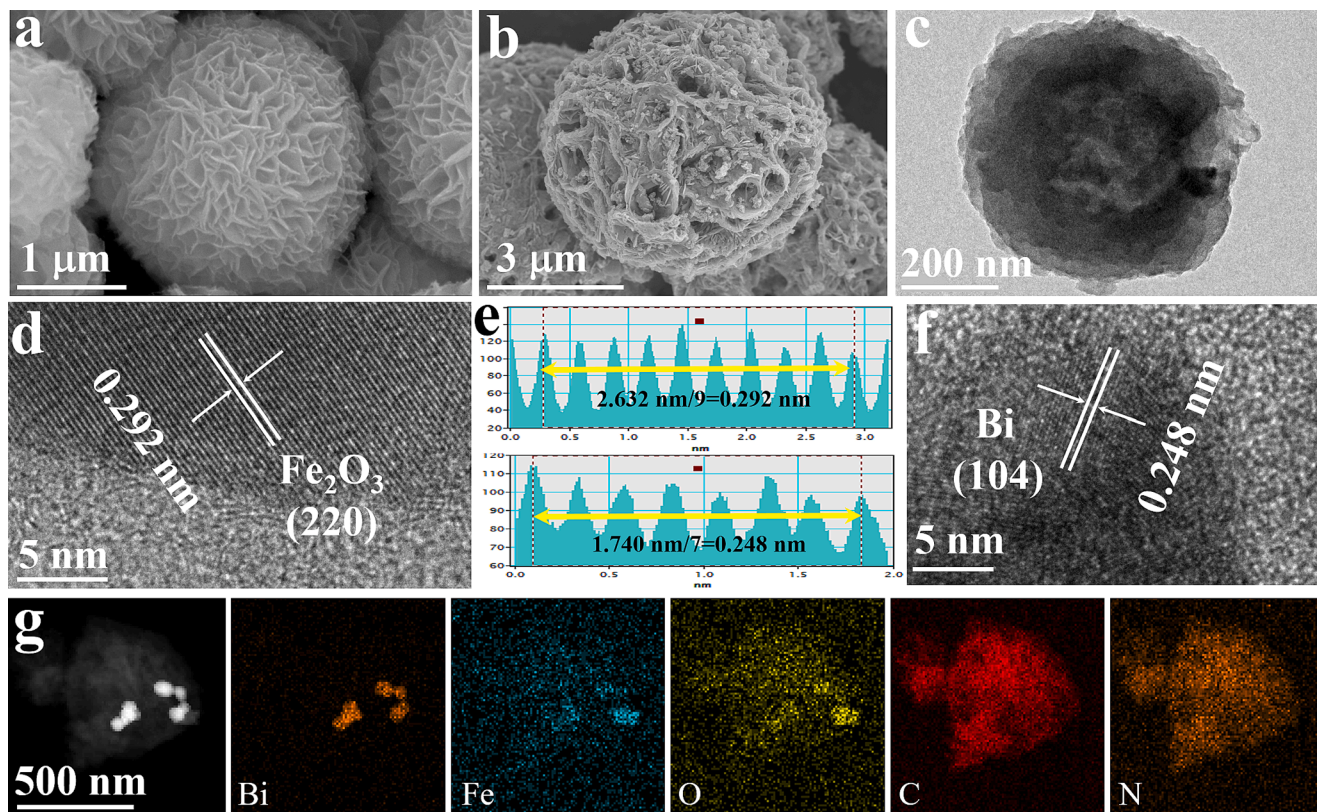
Fig. 2. (a) SEM image of BiOBr precursor. (b) SEM image, (c) TEM image, (d-f) HR-TEM image, and (g) HAADF-STEM images and the corresponding elemental mappings of Bi-Fe$_2$O$_3$@NC.

chemical states of the synthesized catalysts, X-ray photoelectron spectroscopy (XPS) analysis was conducted. The XPS survey spectrum confirmed the existence of Bi, Fe, C, N, and O in various catalysts (Fig. S7), which is consistent with the EDS-mapping results. The C 1s spectrum of Bi-Fe$_2$O$_3$@NC (Fig. S8) exhibited four distinct peaks at 284.0 (C=C), 284.8 (C—C), 286.0 (C—O) and 289.3 eV (C=O), respectively [36]. The Fe 2p$_{3/2}$ core level of Bi-Fe$_2$O$_3$@NC can be separated into two peaks at 712.8 and 720.5 eV, corresponding to Fe^{3+}

species and satellite peak, respectively [37]. In contrast, the Fe-Fe$_3$O$_4$@NC spectrum exhibited four peaks at 709.3, 710.5, 712.8 and 718.0 eV, assigned to Fe^0, Fe^{2+}, Fe^{3+}, and satellite peak of Fe 2p$_{3/2}$, consistent with the XRD results (Fig. 3a) [38]. Notably, the Bi 4f high-resolution spectrum displayed two peaks at 157.2 and 162.5 eV, corresponding to Bi 4f$_{7/2}$ and Bi 4f$_{5/2}$ of metallic Bi^0, confirming the presence of metallic Bi in Bi-Fe$_2$O$_3$@NC (Fig. 3b) [39]. In contrast, the peaks observed at 158.9 and 164.1 eV correspond to Bi^{3+} of Bi 4f$_{7/2}$ and Bi 4f$_{5/}$
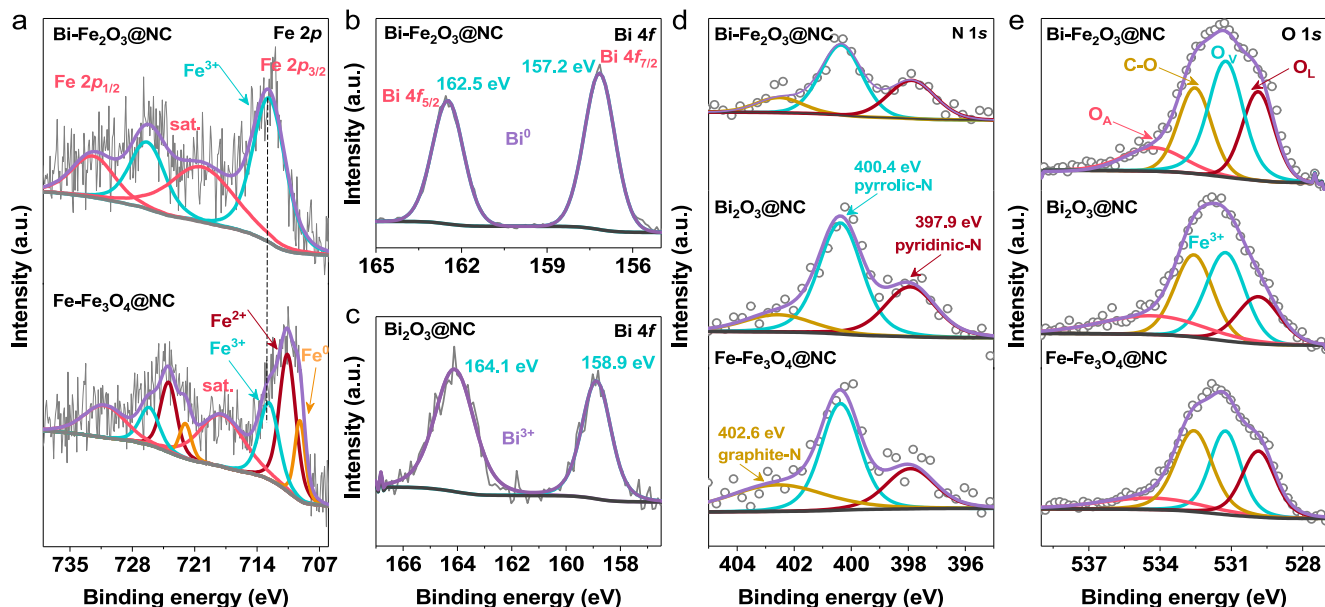

Fig. 3. High-resolution XPS spectra of (a) Fe 2p, (b-c) Bi 4f, (d) N 1s, and (e) O 1s in as-synthesized samples.

$_2$ in $Bi_2O_3@NC$ (Fig. 3c) [40,41]. The Bi-$Fe_2O_3@NC$ composite comprises Bi^0 and Fe^{3+} ions, with Bi^0 acting as an electron donor, providing more catalytic active sites and significantly elevating the catalytic activity. Moreover, the N 1s XPS spectra displayed three typical peaks attributed to pyridinic-N (397.9 eV), pyrrolic-N (400.4 eV), and graphite-N (402.6 eV) in Bi-$Fe_2O_3@NC$, $Bi_2O_3@NC$, and Fe-$Fe_3O_4@NC$, confirming successful *N*-doping during the high temperature calcination treatment (Fig. 3c) [42]. The O 1s high-resolution spectra (Fig. 3d) could be deconvoluted into four characteristic peaks, including lattice oxygen (O_L), oxygen vacancies (O_V), C—O bond, and surface adsorbed oxygen species (O_A), respectively [43]. The presence of oxygen vacancies is consistent with the EPR results.

3.2. ORR activity in alkaline media

The ORR performance of the obtained catalysts was evaluated using the rotating disk electrode (RDE) and rotating ring disk electrodes (RRDE) techniques in O_2/N_2-saturated 0.1 M KOH electrolyte. To optimize the catalyst performance, different concentrations of encapsulated Fe and varying calcination temperatures were employed, as shown in Figs. S9-10, which present the corresponding performance parameters. Among the catalysts, the Bi-$Fe_2O_3@NC$ demonstrated a more positive half-wave potential and limiting current density when the amount of $FeCl_3$ and the pyrolysis temperature were 0.2 M and 900 °C, respectively. Hence, unless stated otherwise, the catalyst with the best performance from the optimization process was selected for further discussion. Distinct cathodic peaks were observed for all samples under O_2 saturated electrolyte compared to N_2 saturated solution, indicating an effective ORR process (Fig. 4a). The cyclic voltammetry (CV) curve of Bi-$Fe_2O_3@NC$ displayed a clear oxygen reduction peak at 0.78 V, surpassing that of Pt/C (0.75 V), and further confirming its superior catalytic activity for ORR [44]. Furthermore, the linear sweep voltammetry (LSV) curves are presented in Fig. 4b. Bi-$Fe_2O_3@NC$ exhibited an onset potential (E_{onset}) of 1.03 V and a half-wave potential ($E_{1/2}$) of 0.88 V, outperforming other control catalysts, including Fe-$Fe_3O_4@NC$ (1.01 V, 0.85 V), $Bi_2O_3@NC$ (0.94 V, 0.82 V) and even Pt/C (1.01 V, 0.84 V). The ultimate current density of Bi-$Fe_2O_3@NC$ exceeded that of the commercial 20% Pt/C (4.9 mA cm^{-2}). Notably, $Bi_2O_3@NC$ catalyst demonstrates a redox peak at approximately 0.4 V (vs. RHE), which can be

attributed to a valence state transition between Bi^{3+} and Bi^{5+} under high potential conditions. Furthermore, the CV curves (Fig. S11) of $Bi_2O_3@NC$ in both N_2 and O_2-saturated electrolytes exhibited a redox peak, providing additional evidence of the intrinsic redox activity of $Bi_2O_3@NC$ [45]. In addition, the kinetic current density (J_k) of Bi-$Fe_2O_3@NC$ reached 34.2 mA cm^{-2} at 0.8 V (Fig. 4c), outperforming $Bi_2O_3@NC$ (7.27 mA cm^{-2}), Fe-$Fe_3O_4@NC$ (9.48 mA cm^{-2}) and commercial Pt/C (10.63 mA cm^{-2}). The remarkable ORR activity of Bi-$Fe_2O_3@NC$ was further evidenced by the lowest Tafel slope (76.2 mV dec^{-1}), lower than $Bi_2O_3@NC$ (87.0 mV dec^{-1}) and Fe-$Fe_3O_4@NC$ (95.4 mV dec^{-1}), and comparable to commercial Pt/C catalysts (96.5 mV dec^{-1}), indicating fast ORR kinetics (Fig. 4d) [46]. The LSV curves of Bi-$Fe_2O_3@NC$ at various rotational speeds from 400 to 2025 rpm are presented in Fig. 4e. The current density increased with higher rotating rates, in accordance with the First order-dynamic equation [47]. The electron transfer number (*n*) for the ORR was determined by calculating the Koutecky-Levith (K-L) slope at different potentials (inset of Fig. 4e). The average electron transfer number of Bi-$Fe_2O_3@NC$ was approximately 3.7, confirming that oxygen can be reduced through a direct four-electron pathway [44]. Furthermore, according to the data validated by the rotating ring disk electrode (RRDE) technique, the calculated H_2O_2 yield is below 20% in the potential range of 0.2–0.8 V vs. RHE, and the *n* values were close to 4, except for a single $Bi_2O_3@NC$, further supporting the ideal four-electron pathway for Bi-$Fe_2O_3@NC$ (Fig. 4f) [48]. Moreover, the activity of Bi-$Fe_2O_3@NC$ surpassed most non-precious metal ORR catalysts (Table S1), highlighting its potential as a promising substitute for precious catalysts.

The double-layer capacitance (C_{dl}) serves as a crucial parameter for assessing the active sites on catalyst surface. To determine the C_{dl} values, CV measurements were conducted at varying scan rates within the non-Faraday potential interval (Fig. S12), as the C_{dl} is linearly correlated with the electrochemically active surface area (ECSA). As shown in Fig. 5a, Bi-$Fe_2O_3@NC$ exhibited the highest C_{dl} value of 18.14 mF cm^{-2}, surpassing Fe-$Fe_3O_4@NC$ (6.12 mF cm^{-2}) and $Bi_2O_3@NC$ (1.08 mF cm^{-2}). These findings indicate that Bi-$Fe_2O_3@NC$ possesses a larger ECSA, exposing more active sites to enhance ORR activity [49]. Subsequently, the ECSA was further confirmed by performing CV tests in a mixture of 0.5 mM $K_3[Fe(CN)_6]$ and 0.1 M KCl at different scanning speeds (Fig. S13). In the CV curves of all samples, except $Bi_2O_3@NC$, a
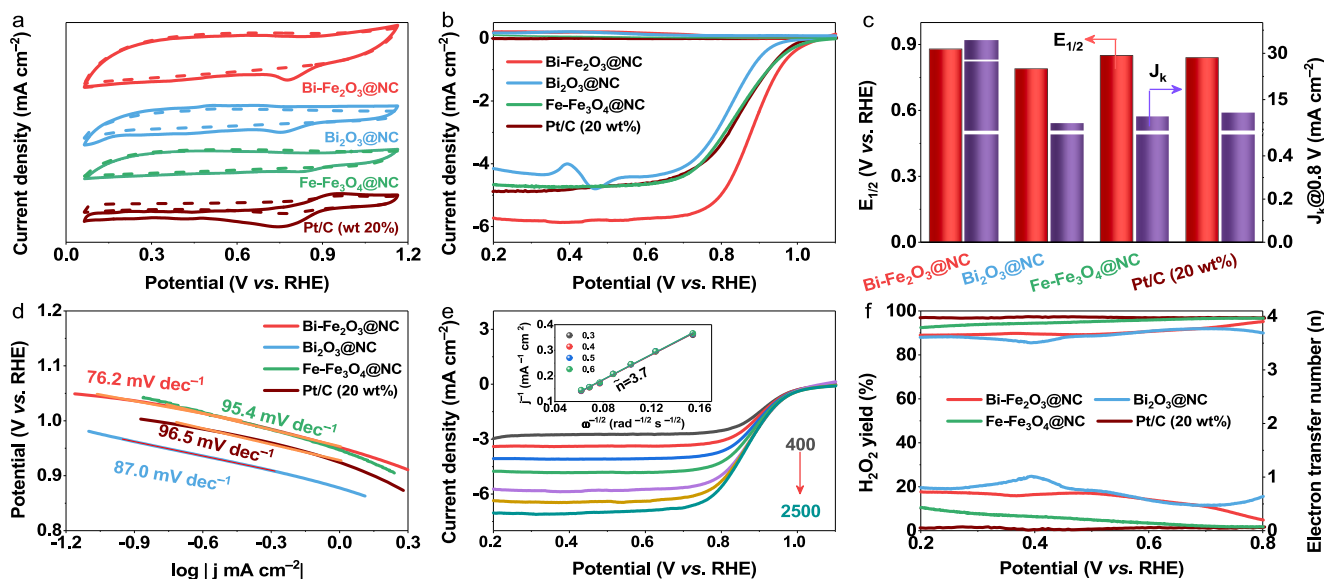

Fig. 4. Electrochemical performance of different catalysts. (a) CV curves in N_2 or O_2-saturated 0.1 M KOH solution. (b) LSV polarization curves in O_2-saturated 0.1 M KOH electrolyte, and (c) the corresponding half-wave potential ($E_{1/2}$) and kinetic current density (J_k) at 0.9 V. (d) Polarization curves of Bi-$Fe_2O_3@NC$ with various rotating speeds from 400 to 2500 rpm and the corresponding K-L plots (inset). (e) Tafel plots and (f) H_2O_2 yield (%) and electron transfer number (*n*) from various catalysts.
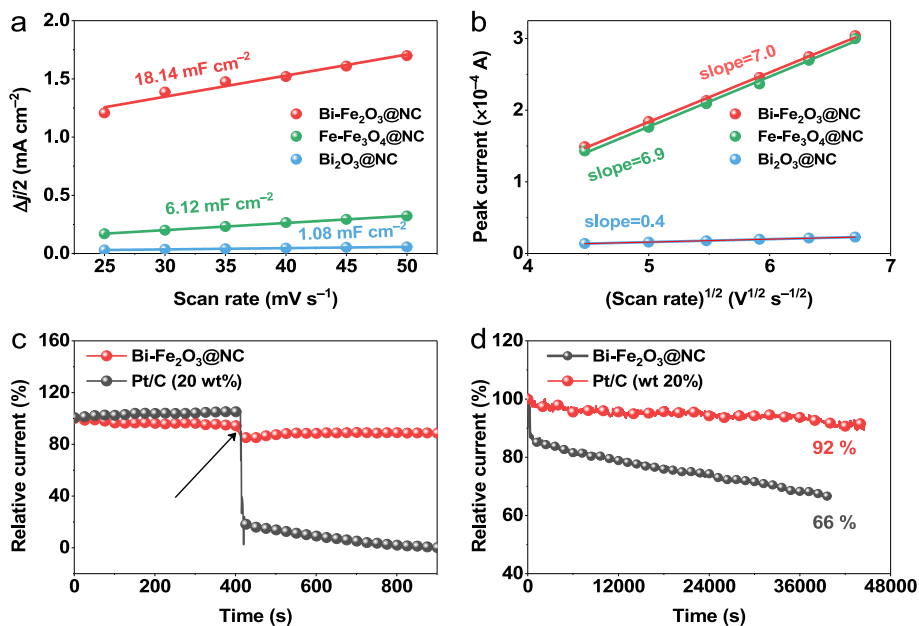
Fig. 5. (a) Double-layer capacitance (C_{dl}) values of Bi-Fe$_2$O$_3$@NC, Fe-Fe$_3$O$_4$@NC, and Bi$_2$O$_3$@NC. (b) CV fitting curves in 0.1 M KCl containing 5 mM K$_3$[Fe(CN)$_6$] solution at various scan rates. (c) Methanol tolerance tests of Bi-Fe$_2$O$_3$@NC and Pt/C (20 wt%) in 0.1 M KOH with the addition of 3 M methanol at around 400 s, and (d) the corresponding stability test in O$_2$-saturated 0.1 M KOH solution at a rotating speed of 1600 rpm.
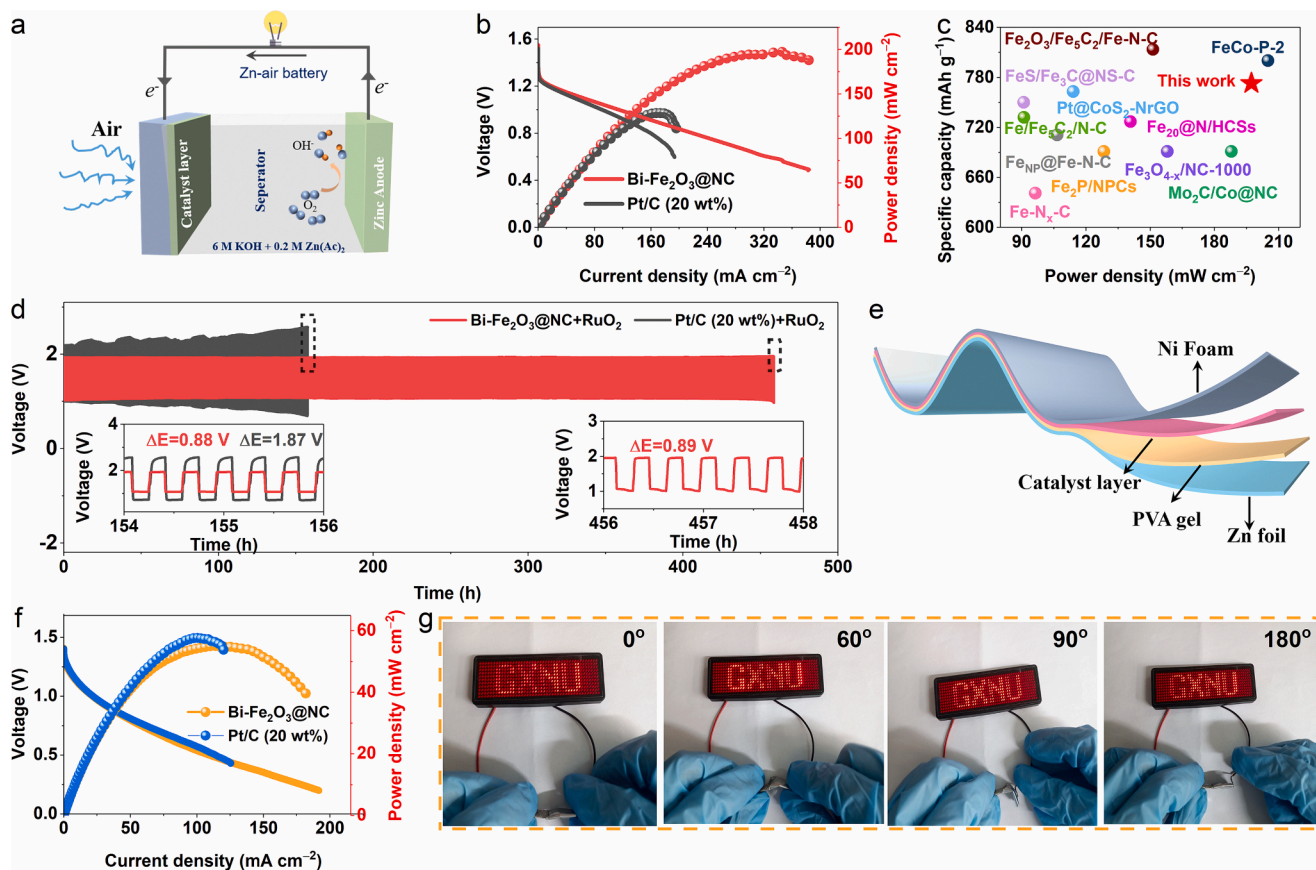

Fig. 6. (a) Schematic configuration of assembled aqueous ZAB. (b) Discharge polarization curves and the corresponding power densities of the ZAB. (c) Comparison of Bi-Fe$_2$O$_3$@NC as air cathode with other recently reported excellent catalysts, in terms of specific capacity and power density. (d) Galvanostatic cycling at 5 mA cm^{-2} (20 min for each cycle). (e) Sketch diagram of the flexible ZAB. (f) The discharge polarization and corresponding power density profiles of Bi-Fe$_2$O$_3$@NC and Pt/C (20 wt%)-based flexible ZABs. (g) Photographs of Bi-Fe$_2$O$_3$@NC-based flexible ZAB powered by LED panel at different bending angles.

distinct pair of redox peaks was observed. The corresponding fitted CV curves, as shown in Fig. 5b, align with the C_{dl} trend, confirming that Bi-Fe$_2$O$_3$@NC exhibits a higher ECSA compared to other catalysts.

To evaluate the stability and methanol resistance, a chronoamperometric response test was conducted at 1600 rpm in an O$_2$ saturated 0.1 M KOH electrolyte. As depicted in Fig. 5c, Bi-Fe$_2$O$_3$@NC maintained a constant current density even after rapid injection of 3 M methanol into the electrolyte at 400 s, whereas the current density of Pt/C significantly decreased, indicating the high methanol resistance of Bi-Fe$_2$O$_3$@NC [50]. Moreover, the current density of Bi-Fe$_2$O$_3$@NC retained 92% of its initial value after approximately 44000 s, while commercial Pt/C maintained 66% at about 40000 s (Fig. 5d). The exceptional durability and methanol tolerance of Bi-Fe$_2$O$_3$@NC can be attributed to its robust multi-channel layered mesoporous structure and the abundant oxygen vacancies within Bi-Fe$_2$O$_3$@NC.

3.3. Test for performance of assembled ZABs

ZABs are highly regarded as promising energy storage systems due to their exceptional cleanliness, high efficiency, and safety. To evaluate the practicality of Bi-Fe$_2$O$_3$@NC, its remarkable ORR performance has been explored in alkaline ZABs. Fig. 6a presents a schematic diagram of the ZAB. As shown in Fig. S14a-b, the Bi-Fe$_2$O$_3$@NC-based ZAB exhibited a higher open circuit voltage (OCV) of 1.55 V and specific capacity of 774.3 mAh g_{Zn}^{-1}) compared to the Pt/C-based ZAB (OCV of 1.48 V, specific capacity of 700.9 mAh g_{Zn}^{-1}). Notably, the liquid ZAB based on Bi-Fe$_2$O$_3$@NC achieved an impressive peak power density of 198.6 mW cm^{-2} (Fig. 6b), significantly outperforming Pt/C + RuO$_2$ at 132.4 mW cm^{-2}. Satisfactorily, the Bi-Fe$_2$O$_3$@NC-based ZAB exhibited higher OCV, maximum power density, and specific capacity compared to recently reported ZABs (Fig. 6c and Table S2). The discharge curves of Bi-Fe$_2$O$_3$@NC-based ZAB showed negligible voltage drop at various current densities (Fig. S14c), indicating exceptional rate performance and reversibility [51]. Stability tests were performed at 5 mA cm^{-2} to investigate the cycle life of the ZAB. The Bi-Fe$_2$O$_3$@NC-based ZAB operated continuously for 459 h with a negligible charge/discharge voltage gap (ΔE) (Fig. 6d). In contrast, the Pt/C-based ZAB significantly declined after only 158 h, demonstrating the superior round-trip efficiency of the former. Significantly, a sandwich-structured all-solid-state ZAB was assembled to explore the feasibility of Bi-Fe$_2$O$_3$@NC as an air electrode for flexible devices, as illustrated in Fig. 6e. The flexible ZAB based on Bi-Fe$_2$O$_3$@NC exhibited an impressive OCV of 1.32 V (Fig. S15). Apparently, the Bi-Fe$_2$O$_3$@NC-based flexible ZAB provided a maximum power density of 55.9 mW cm^{-2} (Fig. 6f), surpassing most recently reported solid state ZABs (Table S3). These results highlight the tremendous potential of Bi-Fe$_2$O$_3$@NC as a viable alternative for powering flexible ZAB devices. Furthermore, the flexibility of the Bi-Fe$_2$O$_3$@NC-based flexible ZAB device was demonstrated by measuring its performance in both an unbent state and at various bending angles (30°, 60°, 90°, and 180°) to power a red LED display, suggesting its potential application under external mechanical stress (Fig. 6g) [52]. These results underscore the significant potential of Bi-Fe$_2$O$_3$@NC in practical energy conversion applications.

The exceptional ORR catalytic activity and ultrahigh durability of Bi-Fe$_2$O$_3$@NC can be attributed to the compositional synergy and architectural advantages resulting from the following aspects: (i) The inclusion of metallic Bi in the Bi-Fe$_2$O$_3$@NC composite serves to enhance electrical conductivity and expedite electron transfer processes. Simultaneously, Fe$_2$O$_3$ promotes the adsorption of oxygen-containing reaction intermediates, consequently reducing the reaction energy barrier [53]. Additionally, the NC skeleton protects the active site, improves the stability of the catalyst, and synergistically enhances the ORR kinetics; (ii) Abundant oxygen vacancies regulate the electronic structure and provide new active sites on the catalyst surface during the ORR process [54]; (iii) The unique multi-channel mesoporous structure enhances

electrode–electrolyte contact and provides an effective pathway for rapid electron/mass transfer [55,56]; (iv) The surface-wrinkled microspheres expose more catalytic active site, accelerating mass transfer and achieving high ORR electrocatalytic performance.

4. Conclusions

In conclusion, the Bi-Fe$_2$O$_3$@NC catalyst exhibits exceptional performance and shows promising potential for various energy conversion applications. Its outstanding ORR catalytic activity, along with its ultrahigh durability and flexibility, make it a highly desirable candidate for alkaline ZABs and solid-state ZAB devices. The Bi-Fe$_2$O$_3$@NC-based ZAB demonstrates higher open circuit voltage, specific capacity, and peak power density compared to traditional Pt/C-based systems, along with excellent rate performance and reversibility. Moreover, the Bi-Fe$_2$O$_3$@NC-based ZAB exhibits superior stability and round-trip efficiency, making it a reliable energy storage solution. Furthermore, the flexibility of the Bi-Fe$_2$O$_3$@NC-based ZAB device enables its application under external mechanical stress, opening up possibilities for powering flexible devices. The exceptional performance of Bi-Fe$_2$O$_3$@NC can be attributed to its compositional synergy, including the role of metallic Bi and Fe$_2$O$_3$ in enhancing conductivity, promoting electron transfer, and reducing the energy barrier for ORR. The NC skeleton provides stability, while the presence of oxygen vacancies and the unique mesoporous structure contribute to enhanced electrocatalytic performance. Overall, the promising properties of Bi-Fe$_2$O$_3$@NC make it a highly favorable catalyst for practical energy conversion applications.

CRediT authorship contribution statement

Lixia Wang: Investigation, Conceptualization, Writing – original draft. **Yanjing Qin:** Investigation. **Huatong Li:** Data curation. **Zhiyang Huang:** Methodology. **Mingcheng Gao:** Data curation. **Tayirjan Taylor Isimjan:** Writing – review & editing. **Xiulin Yang:** Supervision, Writing – review & editing.

Declaration of Competing Interest

The authors declare that they have no known competing financial interests or personal relationships that could have appeared to influence the work reported in this paper.

Data availability

No data was used for the research described in the article.

Acknowledgements

Appendix A. Supplementary data

Supplementary data to this article can be found online at https://doi.org/10.1016/j.jcis.2023.07.033.

References

[1] H. Hu, Y. Meng, Y. Mei, P.X. Hou, C. Liu, H.M. Cheng, M. Shao, J.C. Li, Bifunctional oxygen electrocatalysts enriched with single Fe atoms and NiFe$_2$O$_4$ nanoparticles for rechargeable zinc–air batteries, Energy Storage Mater. 54 (2023) 517–523, https://doi.org/10.1016/j.ensm.2022.11.001.

[2] X. Yang, Z. Zhou, Y. Zou, J. Kuang, D. Ye, S. Zhang, Q. Gao, S. Yang, X. Cai, Y. Fang, Interface reinforced 2D/2D heterostructure of Cu-Co oxides/FeCo hydroxides as monolithic multifunctional catalysts for rechargeable/flexible zinc-air batteries and self-powered water splitting, Appl. Catal. B Environ. 325 (2023), 122332, https://doi.org/10.1016/j.apcatb.2022.122332.

[3] S. Ramakrishnan, D.B. Velusamy, S. Sengodan, G. Nagaraju, D.H. Kim, A.R. Kim, D. J. Yoo, Rational design of multifunctional electrocatalyst: An approach towards efficient overall water splitting and rechargeable flexible solid-state zinc–air battery, Appl. Catal. B: Environ. 300 (2022), 120752, https://doi.org/10.1016/j.apcatb.2021.120752.

[4] R. Ma, X. Cui, X. Xu, Y. Wang, G. Xiang, L. Gao, Z. Lin, Y. Yang, Collaborative integration of ultrafine Fe2P nanocrystals into Fe, N, P-codoped carbon nanoshells for highly-efficient oxygen reduction, Nano Energy 108 (2023), 108179, https://doi.org/10.1016/j.nanoen.2023.108179.

[5] W. Xie, Y. Liu, Y. Yan, M. Yang, M. Zhang, B. Liu, H. Li, H. Chen, Z. Lin, Metal-mediated Schiff base polymer enables metal/nitrogen codoped carbon nanosheets as efficient bifunctional electrocatalyst for durable rechargeable Zn-air batteries, Energy Storage Mater. 59 (2023), 102783, https://doi.org/10.1016/j.ensm.2023.102783.

[6] L. Gong, J. Zhu, F. Xia, Y. Zhang, W. Shi, L. Chen, J. Yu, J. Wu, S. Mu, Marriage of Ultralow Platinum and Single-Atom MnN4 Moiety for Augmented ORR and HER Catalysis, ACS Catal. 13 (2023) 4012–4020, https://doi.org/10.1021/acscatal.2c06340.

[7] M. Cao, Y. Liu, K. Sun, H. Li, X. Lin, P. Zhang, L. Zhou, A. Wang, S. Mehdi, X. Wu, J. Jiang, B. Li, Coupling Fe3C Nanoparticles and N-Doping on Wood-Derived Carbon to Construct Reversible Cathode for Zn–Air Batteries, Small 18 (2022) 2202014, https://doi.org/10.1002/smll.202202014.

[8] Q. Dong, G. Li, F. Liu, J. Ren, H. Wang, R. Wang, Cu nanoclusters activating ultrafine Fe3N nanoparticles via the Mott-Schottky effect for rechargeable zinc-air batteries, Appl. Catal. B Environ. 326 (2023), 122415, https://doi.org/10.1016/j.apcatb.2023.122415.

[9] J. Li, P. Liu, J. Yan, H. Huang, W. Song, Fully-Conjugated Covalent Organic Frameworks with Two Metal Sites for Oxygen Electrocatalysis and Zn–Air Battery, Adv. Sci. 10 (2023) 2206165, https://doi.org/10.1002/advs.202206165.

[10] J. Li, Y. Kang, Z. Lei, P. Liu, Well-controlled 3D flower-like CoP2/CeO2/C heterostructures as bifunctional oxygen electrocatalysts for rechargeable Zn-air batteries, Appl. Catal. B Environ. 321 (2023), 122029, https://doi.org/10.1016/j.apcatb.2022.122029.

[11] H. Tian, X. Cui, H. Dong, G. Meng, F. Kong, Y. Chen, L. Peng, C. Chen, Z. Chang, J. Shi, Engineering single MnN4 atomic active sites on polydopamine-modified helical carbon tubes towards efficient oxygen reduction, Energy Storage Mater. 37 (2021) 274–282, https://doi.org/10.1016/j.ensm.2021.02.017.

[12] M. Guo, Z. Huang, Y. Qu, L. Wang, H. Li, T.T. Isimjan, X. Yang, Synergistic effect and nanostructure engineering of three-dimensionally hollow mesoporous spherical Cu3P/TiO2 in aqueous/flexible Zn–air batteries, Appl. Catal. B Environ. 320 (2023), 121991, https://doi.org/10.1016/j.apcatb.2022.121991.

[13] Y. Deng, X. Tian, G. Shen, Y. Gao, C. Lin, L. Ling, F. Cheng, S. Liao, S. Zhang, Coupling hollow Fe3O4 nanoparticles with oxygen vacancy on mesoporous carbon as a high-efficiency ORR electrocatalyst for Zn-air battery, J. Colloid Interface Sci. 567 (2020) 410–418, https://doi.org/10.1016/j.jcis.2020.02.013.

[14] J. Yan, Y. Huang, Y. Zhang, W. Peng, S. Xia, J. Yu, B. Ding, Facile Synthesis of Bimetallic Fluoride Heterojunctions on Defect-Enriched Porous Carbon Nanofibers for Efficient ORR Catalysts, Nano Lett. 21 (2021) 2618–2624, https://doi.org/10.1021/acs.nanolett.1c00242.

[15] Q. Zhou, S. Hou, Y. Cheng, R. Sun, W. Shen, R. Tian, J. Yang, H. Pang, L. Xu, K. Huang, Y. Tang, Interfacial engineering Co and MnO within N, S co-doped carbon hierarchical branched superstructures toward high-efficiency electrocatalytic oxygen reduction for robust Zn-air batteries, Appl. Catal. B: Environ. 295 (2021), 120281, https://doi.org/10.1016/j.apcatb.2021.120281.

[16] B. Wang, M. Zhang, X. Cui, Z. Wang, M. Rager, Y. Yang, Z. Zou, Z.L. Wang, Z. Lin, Unconventional Route to Oxygen-Vacancy-Enabled Highly Efficient Electron Extraction and Transport in Perovskite Solar Cells, Angew. Chem. Int. Ed. 59 (2020) 1611–1618, https://doi.org/10.1002/anie.201910471.

[17] Y. Zhang, P. Chen, Q. Wang, Q. Wang, K. Zhu, K. Ye, G. Wang, D. Cao, J. Yan, Q. Zhang, High-Capacity and Kinetically Accelerated Lithium Storage in MoO3 Enabled by Oxygen Vacancies and Heterostructure, Adv. Energy Mater. 11 (2021) 2101712, https://doi.org/10.1002/aenm.202101712.

[18] Y. Go, K. Min, H. An, K. Kim, S. Eun Shim, S.-H. Baeck, Oxygen-vacancy-rich CoFe/CoFe2O4 embedded in N-doped hollow carbon spheres as a highly efficient bifunctional electrocatalyst for Zn–air batteries, Chem. Eng. J. 448 (2022) 137665, https://doi.org/10.1016/j.cej.2022.137665.

[19] M. Wu, G. Zhang, H. Tong, X. Liu, L. Du, N. Chen, J. Wang, T. Sun, T. Regier, S. Sun, Cobalt (II) oxide nanosheets with rich oxygen vacancies as highly efficient bifunctional catalysts for ultra-stable rechargeable Zn-air flow battery, Nano Energy 79 (2021), 105409, https://doi.org/10.1016/j.nanoen.2020.105409.

[20] K. Ding, Y. Ye, J. Hu, L. Zhao, W. Jin, J. Luo, S. Cai, B. Weng, G. Zou, H. Hou, X. Ji, Aerophilic Triphase Interface Tuned by Carbon Dots Driving Durable and Flexible Rechargeable Zn-Air Batteries, Nano-Micro Lett. 15 (2023) 28, https://doi.org/10.1007/s40820-022-00994-3.

[21] W. Cheng, X.F. Lu, D. Luan, X.W.D. Lou, NiMn-Based Bimetal-Organic Framework Nanosheets Supported on Multi-Channel Carbon Fibers for Efficient Oxygen Electrocatalysis, Angew. Chem. Int. Ed. 41 (2020) 18234–18239, https://doi.org/10.1002/anie.202008129.

[22] Y. Gao, D. Zheng, Q. Li, W. Xiao, T. Ma, Y. Fu, Z. Wu, L. Wang, 3D Co3O4-RuO2 Hollow Spheres with Abundant Interfaces as Advanced Trifunctional

[22] Electrocatalyst for Water-Splitting and Flexible Zn–Air Battery, Adv. Funct. Mater. 32 (2022) 2203206, https://doi.org/10.1002/adfm.202203206.

[23] H. Xia, Z. Zhang, J. Liu, X. Ning, S. Zhang, X. Lu, Developing superior catalysts engineered by multichannel healing strategy for advanced oxidation, Appl. Catal. B: Environ. 250 (2019) 189–199, https://doi.org/10.1016/j.apcatb.2019.03.033.

[24] Y. Huang, X. Hu, J. Li, J. Zhang, D. Cai, B. Sa, H. Zhan, Z. Wen, Rational construction of heterostructured core-shell Bi2S3@Co9S8 complex hollow particles toward high-performance Li- and Na-ion storage, Energy Storage Mater. 29 (2020) 121–130, https://doi.org/10.1016/j.ensm.2020.04.004.

[25] L. Xu, Y. Xie, L. Li, Z. Hu, Y. Wang, J.C. Yu, Highly selective photocatalytic synthesis of ethylene-derived commodity chemicals on BiOBr nanosheets, Mater. Today Phys. 21 (2021), 100551, https://doi.org/10.1016/j.mtphys.2021.100551.

[26] S. Arya Gopal, A. Edathiparambil Poulose, C. Sudakar, A. Muthukrishnan, Kinetic Insights into the Mechanism of Oxygen Reduction Reaction on Fe2O3/C Composites, ACS Appl. Mater. Interfaces 13 (2021) 44195–44206, https://doi.org/10.1021/acsami.1c10114.

[27] C. Xu, C. Guo, J. Liu, B. Hu, J. Dai, M. Wang, R. Jin, Z. Luo, H. Li, C. Chen, Accelerating the oxygen adsorption kinetics to regulate the oxygen reduction catalysis via Fe3C nanoparticles coupled with single Fe-N4 sites, Energy Storage Mater. 51 (2022) 149–158, https://doi.org/10.1016/j.ensm.2022.06.038.

[28] Y. Liu, L. Ojamäe, C-C Stretching Raman Spectra and Stabilities of Hydrocarbon Molecules in Natural Gas Hydrates: A Quantum Chemical Study, J. Phys. Chem. A 118 (2014) 11641–11651, https://doi.org/10.1021/jp501118p.

[29] R. Balaji, T.T. Nguyen, M.P. Austeria, D.H. Kim, J.H. Lee, N.H. Kim, Electronic coupling coordinated vanadium nitride/magnesium oxide hetero-junction for accelerating oxygen reaction and long-life flexible zinc-air batteries, Appl. Catal. B: Environ. 335 (2023) 122895, https://doi.org/10.1016/j.apcatb.2023.122895.

[30] M. Guo, M. Xu, Y. Qu, C. Hu, P. Yan, T.T. Isimjan, X. Yang, Electronic/mass transport increased hollow porous Cu3P/MoP nanospheres with strong electronic interaction for promoting oxygen reduction in Zn-air batteries, Appl. Catal. B: Environ. 297 (2021), 120415, https://doi.org/10.1016/j.apcatb.2021.120415.

[31] X. Dai, Y. Tian, A. Meng, L. Wang, G. Li, J. Huang, X. Yu, S. Ding, Z. Li, Modulating vacancies concentration ratio of cationic and anionic in WO3 for driving high performance magnesium ions storage, Energy Storage Mater. 57 (2023) 125–135, https://doi.org/10.1016/j.ensm.2023.02.014.

[32] G. Cui, Y. Zeng, J. Wu, Y. Guo, G. Li, X.W. Lou, Synthesis of Nitrogen-Doped KMn8O16 with Oxygen Vacancy for Stable Zinc-Ion Batteries, Adv. Sci. 9 (2022) 2106067, https://doi.org/10.1002/advs.202106067.

[33] Y. Lu, Y. Huang, Y. Zhang, J.-J. Cao, H. Li, C. Bian, S.C. Lee, Oxygen vacancy engineering of Bi2O3/Bi2O2CO3 heterojunctions: Implications of the interfacial charge transfer, NO adsorption and removal, Appl. Catal. B Environ. 231 (2018) 357–367, https://doi.org/10.1016/j.apcatb.2018.01.008.

[34] J. Zhang, J. Chen, Y. Luo, Y. Chen, C. Zhang, Y. Luo, Y. Xue, H. Liu, G. Wang, R. Wang, Engineering heterointerfaces coupled with oxygen vacancies in lanthanum–based hollow microspheres for synergistically enhanced oxygen electrocatalysis, J. Energy Chem. 60 (2021) 503–511, https://doi.org/10.1016/j.jechem.2020.11.037.

[35] H. Fu, N. Zhang, F. Lai, L. Zhang, S. Chen, H. Li, K. Jiang, T. Zhu, F. Xu, T. Liu, Surface-Regulated Platinum-Copper Nanoframes in Electrochemical Reforming of Ethanol for Efficient Hydrogen Production, ACS Catal. 12 (2022) 11402–11411, https://doi.org/10.1021/acscatal.2c03022.

[36] Z. Liu, M. Liao, L. Wang, Z. Luo, T.T. Isimjan, X. Yang, Synergistically improved hydrogen evolution by interface engineering of monodispersed Co5.47N/CoMoOx hybrid particles on carbon cloth with rich oxygen vacancies, Chem. Eng. J. 462 (2023) 142281, https://doi.org/10.1016/j.cej.2023.142281.

[37] Y. Deng, Z. Xiao, Z. Wang, J. Lai, X. Liu, D. Zhang, Y. Han, S. Li, W. Sun, L. Wang, The rational adjusting of proton-feeding by Pt-doped FeP/C hollow nanorod for promoting nitrogen reduction kinetics, Appl. Catal. B: Environ. 291 (2021), 120047, https://doi.org/10.1016/j.apcatb.2021.120047.

[38] F. Chen, H. Luo, Y. Cheng, J. Liu, X. Wang, R. Gong, Fe/Fe3O4@N-Doped Carbon Hexagonal Plates Decorated with Ag Nanoparticles for Microwave Absorption, ACS Appl. Mater. Interfaces 2 (2019) 7266–7278, https://doi.org/10.1021/acsanm.9b01755.

[39] D. Jin, J. Ma, R. Sun, Nitrogen-doped biochar nanosheets facilitate charge separation of a Bi/Bi2O3 nanosphere with a Mott-Schottky heterojunction for efficient photocatalytic reforming of biomass, J. Mater. Chem. C 10 (2022) 3500–3509, https://doi.org/10.1039/D1TC05931A.

[40] X. Shao, Y. Yang, Y. Liu, P. Yan, S. Zhou, T. Taylor Isimjan, X. Yang, Oxygen vacancy-rich N-doped carbon encapsulated BiOCl-CNTs heterostructures as robust electrocatalyst synergistically promote oxygen reduction and Zn-air batteries, J. Colloid Interface Sci. 607 (2022) 826–835, https://doi.org/10.1016/j.jcis.2021.08.210.

[41] J. Sun, W. Zheng, S. Lyu, F. He, B. Yang, Z. Li, L. Lei, Y. Hou, Bi/Bi2O3 nanoparticles supported on N-doped reduced graphene oxide for highly efficient CO2 electroreduction to formate, Chin. Chem. Lett. 31 (2020) 1415–1421, https://doi.org/10.1016/j.cclet.2020.04.031.

[42] M. Shen, J. Liu, J. Li, C. Duan, C. Xiong, W. Zhao, L. Dai, Q. Wang, H. Yang, Y. Ni, Breaking the N-limitation with N-enriched porous submicron carbon spheres anchored Fe single-atom catalyst for superior oxygen reduction reaction and Zn-air batteries, Energy Storage Mater. 59 (2023), 102790, https://doi.org/10.1016/j.ensm.2023.102790.

[43] C. Hu, F. Wei, Q. Liang, Q. Peng, Y. Yang, T. Taylor Isimjan, X. Yang, Electronically modulated d-band centers of MOF-derived carbon-supported Ru/HfO2 for oxygen reduction and aqueous/flexible zinc-air batteries, J. Energy Chem. 80 (2023) 247–255, https://doi.org/10.1016/j.jechem.2023.01.047.

[44] R. He, L. Yang, Y. Zhang, X. Wang, S. Lee, T. Zhang, L. Li, Z. Liang, J. Chen, J. Li, A. Ostovari Moghaddam, J. Llorca, M. Ibáñez, J. Arbiol, Y. Xu, A. Cabot, A CrMnFeCoNi high entropy alloy boosting oxygen evolution/reduction reactions and zinc-air battery performance, Energy Storage Mater. 58 (2023) 287–298, https://doi.org/10.1016/j.ensm.2023.03.022.

[45] H. Tian, L. Zeng, Y. Huang, Z. Ma, G. Meng, L. Peng, C. Chen, X. Cui, J. Shi, In Situ Electrochemical Mn(III)/Mn(IV) Generation of Mn(II)O Electrocatalysts for High-Performance Oxygen Reduction, Nano-Micro Lett. 12 (2020) 161, https://doi.org/10.1007/s40820-020-00500-7.

[46] W. Zhai, S. Huang, C. Lu, X. Tang, L. Li, B. Huang, T. Hu, K. Yuan, X. Zhuang, Y. Chen, Simultaneously Integrate Iron Single Atom and Nanocluster Triggered Tandem Effect for Boosting Oxygen Electroreduction, Small 18 (2022) 2107225, https://doi.org/10.1002/smll.202107225.

[47] G. Xing, M. Tong, P. Yu, L. Wang, G. Zhang, C. Tian, H. Fu, Reconstruction of Highly Dense Cu−N₄ Active Sites in Electrocatalytic Oxygen Reduction Characterized by Operando Synchrotron Radiation, Angew. Chem. Int. Ed. 61 (2022), e202211098, https://doi.org/10.1002/anie.202211098.

[48] M. Liu, T.-C. Yang, Z. Pan, J. Lee, L. An, B. Qiu, H. Yin, C.-M. Yang, L.Y.S. Lee, Bridging Li-Ion Batteries and Fuel Cells: From Cathode Leaching Residue to an Atomic-Scale Catalytic System, ACS Energy Lett. 8 (2023) 1652–1661, https://doi.org/10.1021/acsenergylett.3c00109.

[49] R. Gan, Y. Wang, X. Zhang, Y. Song, J. Shi, C. Ma, Edge atomic Fe sites decorated porous graphitic carbon as an efficient bifunctional oxygen catalyst for Zinc-air batteries, J. Energy Chem. (2023), https://doi.org/10.1016/j.jechem.2023.03.056.

[50] Y. Zhao, H. Wu, Y. Wang, L. Liu, W. Qin, S. Liu, J. Liu, Y. Qin, D. Zhang, A. Chu, B. Jia, X. Qu, M. Qin, Sulfur coordination engineering of molybdenum single-atom for dual-functional oxygen reduction/evolution catalysis, Energy Storage Mater. 50 (2022) 186–195, https://doi.org/10.1016/j.ensm.2022.05.015.

[51] X. Zhang, X. Han, Z. Jiang, J. Xu, L. Chen, Y. Xue, A. Nie, Z. Xie, Q. Kuang, L. Zheng, Atomically dispersed hierarchically ordered porous Fe–N–C electrocatalyst for high performance electrocatalytic oxygen reduction in Zn-Air battery, Nano Energy 71 (2020), 104547, https://doi.org/10.1016/j.nanoen.2020.104547.

[52] Z. Pei, Z. Yuan, C. Wang, S. Zhao, J. Fei, L. Wei, J. Chen, C. Wang, R. Qi, Z. Liu, Y. Chen, A Flexible Rechargeable Zinc-Air Battery with Excellent Low-Temperature Adaptability, Angew. Chem. Int. Ed. 59 (2020) 4793–4799, https://doi.org/10.1002/anie.201915836.

[53] K. Li, R. Cheng, Q. Xue, T. Zhao, F. Wang, C. Fu, Construction of a Co/MnO Mott-Schottky Heterostructure to Achieve Interfacial Synergy in the Oxygen Reduction Reaction for Aluminum-Air Batteries, ACS Appl. Mater. Interfaces 15 (2023) 9150–9159, https://doi.org/10.1021/acsami.2c13871.

[54] Y. Tian, X. Liu, L. Xu, D. Yuan, Y. Dou, J. Qiu, H. Li, J. Ma, Y. Wang, D. Su, S. Zhang, Engineering Crystallinity and Oxygen Vacancies of Co(II) Oxide Nanosheets for High Performance and Robust Rechargeable Zn–Air Batteries, Adv. Funct. Mater. 31 (2021) 2101239, https://doi.org/10.1002/adfm.202101239.

[55] G. Zhang, X. Liu, L. Wang, G. Xing, C. Tian, H. Fu, Copper Collector Generated Cu⁺/Cu²⁺ Redox Pair for Enhanced Efficiency and Lifetime of Zn–Ni/Air Hybrid Battery, ACS Nano 16 (2022) 17139–17148, https://doi.org/10.1021/acsnano.2c07542.

[56] Y. Wang, X. Wu, X. Jiang, X. Wu, Y. Tang, D. Sun, G. Fu, Citrulline-induced mesoporous CoS/CoO heterojunction nanorods triggering high-efficiency oxygen electrocatalysis in solid-state Zn-air batteries, Chem. Eng. J. 434 (2022), 134744, https://doi.org/10.1016/j.cej.2022.134744.